Banding Reduction in Electrophotographic Process Using Human Contrast Sensitivity Function Shaped Photoreceptor Velocity Control

Cheng-Lun Chen and George T.-C. Chiu
School of Mechanical Engineering, Purdue University, West Lafayette, Indiana, USA

Jan Allebach✦
School of Electrical and Computer Engineering, Purdue University, West Lafayette, Indiana, USA

This article presents a process control strategy for reducing banding artifact in electrophotographic (EP) process. EP banding was shown to be closely related to the angular velocity fluctuation of the photoreceptor. Proper regulation of the photoreceptor rotational velocity under various process uncertainties and variations will improve EP process stability and reduce the occurrence of visual banding. The proposed closed-loop control strategy is to modulate the main drive motor speed based on the velocity measurement of the photoreceptor. The controller featured two levels of angular velocity regulation. The first level utilized the loop-shaping technique to incorporate the human visual system (HVS) model, i.e., an approximation of the human contrast sensitivity function (CSF), into the feedback loop to eliminate low frequency and non-periodic velocity fluctuations. The second level used an internal model based repetitive controller to reduce the effect of periodic velocity fluctuation. The HVS based loop shaping design is intended for addressing the subjective evaluation of the human visual perception. Experimental result from a low cost 600 dpi EP engine showed significant banding reduction from reflectance measurement as well as subjective evaluation of the printed image.

Journal of Imaging Science and Technology 47: 209–223 (2003)

Introduction

Electrophotography (EP) is the underlying imaging process used in paper copiers and laser printers. A typical EP process is composed of six basic steps: charging, exposure, development, transfer, fusing, and cleaning. For a typical EP process, the print quality will strongly depend on the stability of these basic steps. Researchers have shown that vibration or transmission deviation resulting from various mechanical components within an EP process can potentially degrade the print quality. The effect of eccentricity on multi-gear transmission accuracy for a color laser printer was examined by Kusuda and co-workers.[1] Kawamoto[2–4] developed dynamic and vibration models for polygon mirror scanner motors and the cleaning blades. He and other researchers[5] have also shown that the electrostatic force on the charge roller is another vibration source. Among various image artifacts, halftone banding due to dot gain or scan line spacing variation is one of the most visible artifacts, which appears as periodic light and dark bands across a printed page perpendicular to the process or print direction.

Significant amount of work has devoted to the modeling and analysis of banding in EP process. Burns and co-workers.[6] modeled the effect of independent identically distributed (iid) zero-mean laser dot positioning error on the mean and variance of the exposure error along the process (or slow scan) direction. The analytical results were verified by simulation for two types of laser profiles, i.e., Gaussian and triangular. Their work pointed out that the sensitivity of a laser writer to raster noise strongly depends on the interaction of the laser profile shape and the system modulation transfer function (MTF). The effect of positioning error due to polygon mirror facet-angle variation on the exposure was also investigated. Melnychuck and Shaw[7] modeled the effect of laser dot positioning error on the halftone cell. To analyze reflectance instead of exposure, the nonlinear transformation between exposure and reflectance was simplified by assuming binary material response. Based on this assumption and a thresholding process, they were able to convert the exposure profile for a halftone cell to a rectangular-shaped reflectance profile. Note that although such quantization striped information concerning the effect of position error on individual dots, the error still affects the overall position and width of the halftone cell. Banding coefficient was introduced by Haas[8] to relate the scan-line or feature spacing modulation to the resulted contrast modulation. The dependence of the banding coefficient on halftone dot size was examined for one-dimension spatial models of arbitrary profile and for numerical simulation of a uniform array of superimposed, scan-smeared Gaussian exposures. It was concluded that the smallest banding coefficient is

Original manuscript received October 11, 2002

✦ IS&T Fellow

Corresponding authors: {chenglun, gchiu}@purdue.edu

obtained for the least halftone dot size and the banding coefficient increases hyperbolically for larger halftone dot size. Analytical models of exposure and reflectance modulation due to simple sinusoidal raster position variation were developed by Loce and co-workers.[9,10] In their work, first order approximation of the halftone cell reflectance, which is similar to the thresholding process used by Melnychuck and Shaw[7], was applied on the exposure profile to yield the on and off regions of the halftone cell. It was shown that for low frequency variation, banding is proportional to the fractional spacing error, the halftone frequency, and the raster spacing; and is inversely proportional to the average reflectance of the halftone cell. Although reflectance variation due to scanline spacing fluctuation is shown to be a direct contributor of banding, a model of the human visual system is needed to reflect the actual perceived banding. The contrast sensitivity function (CSF) is one of such models that attempts to capture the modulation transfer function (MTF) of the human visual system in perceiving contrast variations. Several researchers have contributed to the analysis and synthesis of the CSF function that have been used by other researchers to quantify perceived image quality.[11,12] The bandpass-like CSF function reveals the fact that mid-frequency disturbances have greater impact on perceived banding so that a banding reduction scheme should supply its effort mainly on noise or disturbances located in this frequency region.

Typically, the design of EP engines has relied on tightly toleranced components and open-loop design principles. System parameters and operating conditions are carefully modeled, designed and maintained so that the physical process is least affected by disturbances and uncertainties. For example, exposure level is determined so that the photoreceptor is discharged to saturation; large inertia of the photoreceptor motion system is used to reduce motion sensitivity to load variation; very high manufacturing precisions are kept for the key components in the development system. These solutions are costly and limited. Although closed-loop approach has been seen to be used on component level control, e.g., polygon mirror and main drive motor speed regulation. Regulation of each individual subsystem based on local sensory feedback, e.g., velocity from the motor, usually does not guarantee good regulation on the imaging component where the latent image is formed.

In this study, we proposed closing the loop by controlling the actuator using signal feedback from sensors placed on the component of which specific physical quantities are to be regulated. For example, in a monochrome platform, a suitable choice for the actuator and sensor placement would be the main drive motor and the photoreceptor, respectively. Next, the control algorithm should be able to tackle disturbances with control action within the actuator limitation; e.g., without saturating the actuator. Another objective of using closed-loop control is to obtain system robustness, which, by definition, is to reduce system sensitivity to uncertainties such as consumable change and component aging.

Many works have been reported on reducing banding in EP process. They can be categorized into the following four approaches. The first approach[1,13,14] is to design better gear train, i.e., gear meshing or gear pitch, to either reduce transmission error or move the vibration into higher frequency region where human visual system is less sensitive. The second approach[15–18] is to deflect the laser beam in the print or process direction to compensate for the scan-line spacing variation. The third approach[19–23] is to modulate the laser exposure to directly compensate for the absorptance variation due to line spacing error. Using halftone techniques to mask banding artifacts was also investigated in the literatures.[24,25] Improved velocity regulation of the EP process is more of a challenge since the drive motor transmits the power through a set of gear trains to components that also perform other functions of the imaging process, i.e., media transport.

Since the majority of the photoreceptor velocity variation is of known and constant periods that are related to the transmission gearing, repetitive control is a feasible solution to compensate for these periodic disturbances. Repetitive control based systems have been shown to work well for tracking periodic reference commands and rejecting periodic disturbances in regulation applications. The analysis and synthesis of repetitive controllers for continuous time single-input-single-output (SISO) systems were first proposed by Hara and coworkers. and they extended the idea to MIMO systems in 1998.[26] Around the same time, Tomizuka and co-workers[27] addressed the analysis and synthesis of discrete time repetitive controller considering the fact that digital implementation of a repetitive controller is simpler and does not require the controlled plant to be proper.

In this study, a two level closed-loop photoreceptor drum velocity regulation control was proposed to reduce motion induced banding in EP processes. Through system modeling, signal processing, and experimental measurement, banding artifact was shown to strongly related to the transmission quality, e.g., velocity. The proposed compensation strategy is to improve the EP process stability by reducing the sensitivity of the photoreceptor velocity regulation to both periodic and nonperiodic disturbances and manufacturing uncertainties. The proposed drum velocity loop was closed at the photoreceptor angular position through an optical shaft encoder. To account for the effect of the human visual system in interpreting non-periodic and low spatial frequency artifacts, a HVS based loop-shaping controller was designed to incorporate the human CSF into the nominal loop design. The HVS based controller also helped eliminate dc drift as well as provided robustness to the photoreceptor velocity loop. A second level repetitive controller was designed to compensate for the periodic disturbances that are the major contributors to visual banding. With the removal of the dc components of the disturbances by the HVS based controller, the nominal (mean) value of the photoreceptor angular velocity will be fixed. Thus, the fundamental and harmonic frequencies of the periodic disturbances are stationary and the repetitive control algorithm can be applied directly without modification. Effectiveness of the proposed control approach was verified by using a 600 dpi monochrome EP engine. Experimental results showed significant disturbance reduction in the measured velocity and reflectance within the spatial frequency range where human vision is most sensitive to periodic artifacts. Subjective evaluation of the printed images also demonstrated significant improvement.

System Description

Electrophotographic (EP) Process

A brief description of the electrophotographic imaging process is presented here. A detailed discussion of the physics can be found in Schein.[28] The central component in the EP process is the photoreceptor, or based on the material, sometimes called the organic

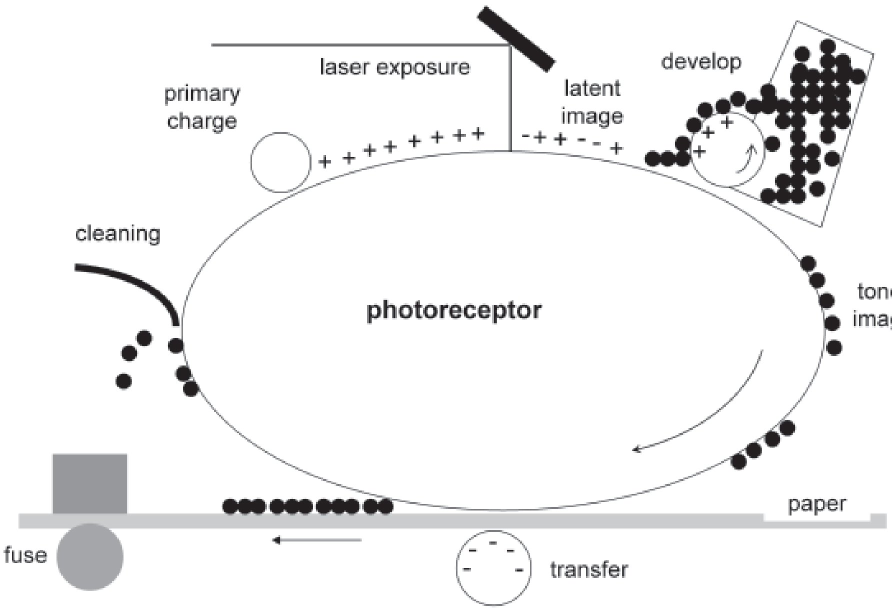

Figure 1. Six basic steps for a typical electrophotographic (EP) process: charging, exposure, developing, transferring, cleaning, and fusing.

photoconductor (OPC), which is in the form of a drum or a belt that continuously rotates and cyclically interacts with several stationary subsystems or processes. The photoreceptor is used as a staging area where a toner image is first built up before being transferred to the paper, or to an intermediate transfer medium. The density profile of the toner image, which is critical to the print quality, depends on the behavior of the following six basic steps (see Fig. 1):

Primary Charge: A primary charge roller applies a DC bias to the photoreceptor. This is usually achieved by placing the photoreceptor near a high voltage corotron wire or roller, which emits charged particles via the coronal discharge process. A uniform charge density is then created on the surface of the photoreceptor. The resulting charge level depends on the voltage and the condition of the corotron wire, the relative motion, and distance between the corotron and the photoreceptor, as well as the voltage on the metal grid.

Laser Exposure: The charged photoreceptor then travels to an exposure station, where a binary operated (either on or off) raster laser beam scans the photoreceptor line by line and emits light at locations where toners are desired (if a discharged area development process is used). Since the photoreceptor is photosensitive, areas where light is shone is discharged. This creates a discharge density profile on the photoreceptor, known as the latent image that resembles the desired image. The depth of the discharge (the discharged well) is affected by the laser power and the nonlinear photo-induced discharged characteristic of the photoreceptor.

Development: In this step, toner particles are deposited on the photoreceptor. Within the development housing, toner particles are pre-charged by being agitated against magnetic carrier beads via the triboelectric process. By biasing the voltage of the development housing with respect to that of the photoreceptor, the charged toner particles are selectively deposited onto the discharged or the charged regions (the latent image) on the photoreceptor. A toner image that corresponds to the desired image is created. The development process depends heavily on the electric field profile in the development gap, as established by the charge profile on the photoreceptor, bias voltages of the development housing, toner charge density, as well as toner surface properties such as cohesivity.

Transfer: In this step, the toner image is transferred to the paper. In general, the photoreceptor is brought in contact with an intermediate medium or a sheet of paper so that the toner particles, which were loosely attached by electrostatic forces to the photoreceptor are deposited onto the medium. This process requires that the intermediate medium or the paper be pre-charged to a sufficiently high potential relative to that of the photoreceptor.

Waste Toner Cleaning: Toner particles that failed to deposit onto the paper is brushed off (electrically and/or mechanically) into the waste toner reservoir by a cleaning blade to avoid contaminating the subsequent images.

Fusing: The final step is the fusing of the toners to the paper. The heat and pressure provided by the fusing assembly serve two purposes: to permanently fuse the toner to the paper, and to melt the toner together to produce the full color image on the page.

The Monochrome EP Process

For a monochrome EP process, the coordination among several motion systems is essential to the final print quality: (see Fig. 2):

- The image formation system, which includes the subsystem responsible for the motion of the photoreceptor, and the subsystem controlling the rastering of the laser beam.
- The pick-up/feed system in charge of paper pick-up and transportation.
- The fusing system.

The first imaging subsystem is usually a motor/gear transmission system composed of a motor, gear trains, and a photosensitive drum or belt. The motor supplies torque to maintain constant angular velocity for the photoreceptor. The velocity of the motor is controlled

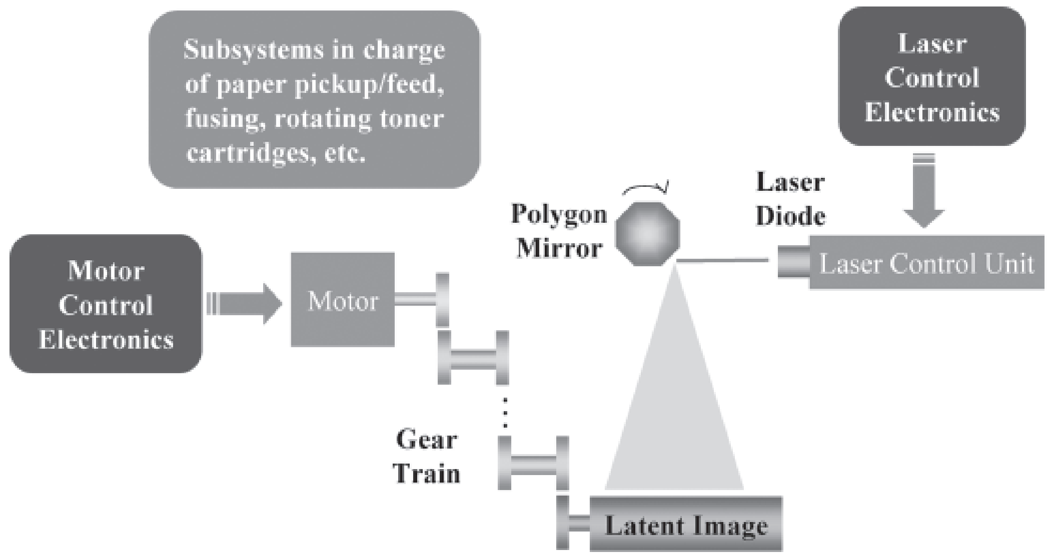

Figure 2. Motion systems that coordinate the sequence of EP processes. The image formation system is composed of the motor/gear transmission subsystem and the laser/polygon mirror subsystem.

through a driver. For stepper motor, the driver generates and repeats a set of stepping sequences, e.g., half or full stepping at certain pre-specified stepping rate such that the motor velocity is proportional to the stepping rate. For brushless dc (BLDC) motor, the driver modulates the amount of currents flowing through the armature windings of the motor by techniques like pulse width modulation (PWM), and thus is able to adjust the motor velocity. The motor shaft drives a set of gear trains that connect with the photoreceptor as well as the corresponding rollers in the EP subsystems.

The second imaging subsystem is the optics part of the EP process, i.e., the laser control unit, the laser diode and the polygon mirror, which deflects the laser beam to the surface of the photoreceptor. Its main task is to control the intensity and location of the laser. The laser control unit generates pulses that control the on–off of the laser diode based on the image that is to be exposed on the photoreceptor.

Nominally, the polygon mirror and the photoreceptor move at constant linear or angular speed by using separate open or closed-loop control, and the laser intensity is preset at certain level. Across-page rastering is achieved by the rotating polygon mirror deflecting the laser beam with the preset intensity from the laser diode across the surface of the photoreceptor, where the scan-line spacing, variation of which induces visual banding, is determined by the motion of the photoreceptor. The motion quality of the photoreceptor thus affects the image quality since it can be affected by mechanical loading and disturbances such as structure vibrations.

System Modeling

As mentioned previously, halftone banding is an artifact due to periodic luminance or reflectance variation on a printed page. Factors that affect either scan-line spacing or dot gain variation are the main contributors to banding. Researchers have shown that vibration or transmission error resulting from mechanical components within an EP system can affect scan-line spacing and thus induce banding. Furthermore, models have also been developed for modeling and analysis of the reflectance variation (banding) due to scan-line spacing variation in EP processes. In the following, we will derive the nonlinear mapping that relates a set of process parameters, i.e., laser scanning frequency, angular velocity of the photoreceptor, and the radius of rotation, to the output reflectance on the printed image.

From Process Parameters to Scan Line Spacing

A rigorous relation among the scan-line spacing, the photoreceptor drum velocity, and the instantaneous radius of rotation can be derived by inspecting Fig. 3, where f_s is the laser beam scanning frequency in Hz and Δl is the scan-line spacing. Suppose at point P, where the laser beam hits the surface of the drum, the instantaneous radius of rotation is r. θ and w are angular position and angular velocity, respectively. From basic geometry, we have

$$dl = \sqrt{(dr)^2 + (rd\theta)^2} \tag{1}$$

which implies that

$$\frac{dl}{d\theta} = \sqrt{\left(\frac{dr}{d\theta}\right)^2 + r^2} \tag{2}$$

or

$$\frac{dl/dt}{d\theta/dt} = \sqrt{\left(\frac{dr}{d\theta}\right)^2 + r^2} \tag{3}$$

Use the fact that $w = d\theta/dt$, we have

$$\frac{dl}{dt} = w\sqrt{\left(\frac{dr}{d\theta}\right)^2 + r^2}\ . \tag{4}$$

Now suppose that (l_0,t_0) is the coordinate pair representing the measured linear displacement at time t_0. The line spacing thus is governed by the following equation:

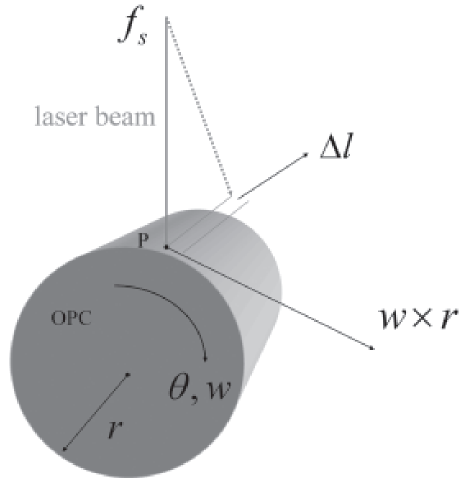

Figure 3. Relationship among scan line spacing, instantaneous radius of rotation, and photoconductive drum velocity.

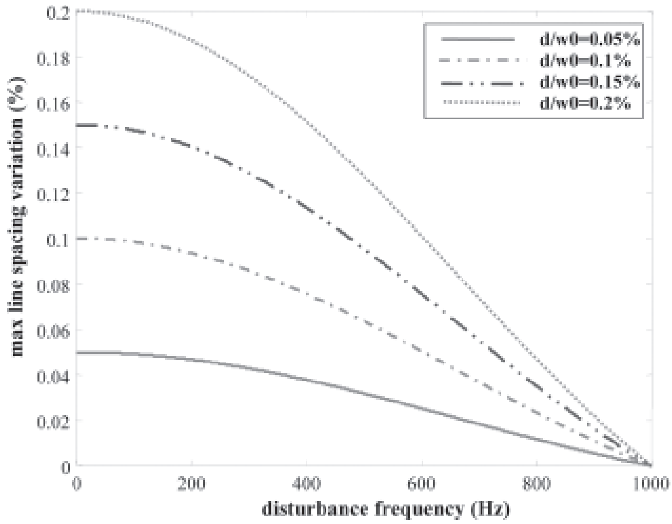

Figure 4. Effect of magnitude and frequency of velocity fluctuation on maximum line spacing variation.

$$\Delta l = \int_{l_0}^{l_0+\Delta l} dl = \int_{t_0}^{t_0+1/f_s} w\sqrt{\left(\frac{dr}{d\theta}\right)^2 + r^2}\, dt \tag{5}$$

Since no assumptions are made on velocity, radius and scanning frequency, Eq. (5) gives a general kinematic relationship among those variables.

Effect of Angular Velocity Variation

To study the effect of angular velocity variation on line spacing, the scanning frequency f_s and the radius of rotation r are assumed to be constant. Without loss of generality, in the subsequent derivation, we will assume that the angular velocity variation can be modeled by a single sinusoidal component. More complicated velocity variation model can be employed but the corresponding result will be much more complex and difficult to analyze. Assume that the nominal drum angular velocity w_0 (rad/s) is augmented by the variation of magnitude d (rad/s), frequency f_d (Hz), and phase ϕ (radians), i.e.,

$$w(t) = w_0 + d\sin(2\pi f_d t + \phi) \ . \tag{6}$$

Substituting Eq. (6) into Eq. (5) yields

$$\begin{aligned}\Delta l &= r_0\int_{t_0}^{t_0+1/f_s}\left[w_0 + d\sin(2\pi f_d t + \phi)\right] dt \\ &= \frac{w_0 r_0}{f_s} + \frac{d r_0}{\pi f_d}\sin\left(2\pi f_d t_0 + \phi + \pi\frac{f_d}{f_s}\right)\sin\left(\pi\frac{f_d}{f_s}\right) \\ &= \frac{w_0 r_0}{f_s} + \frac{d r_0}{f_s}\sin c\left(\pi\frac{f_d}{f_s}\right)\sin\left(2\pi f_d t_0 + \phi + \pi\frac{f_d}{f_s}\right).\end{aligned} \tag{7}$$

Several interesting observations can be made from Eq. (7):

- While the nominal or desired line spacing is $\Delta l_0 = w_0 r_0/f_s$, the maximum line spacing fluctuation is given by

$$\max_t(\Delta l - \Delta l_0) = \frac{d r_0}{f_s}\sin c\left(\pi\frac{f_d}{f_s}\right), \tag{8}$$

which is directly proportional to the magnitude of the velocity variation and the drum radius, but inversely proportional to the laser scanning frequency.

- The velocity variation induces line spacing variation at the same temporal frequency.
- The percent maximum line spacing fluctuation γ_d due to photoreceptor drum velocity variation can be defined as

$$\begin{aligned}\gamma_l &= \frac{\max_t(\Delta l - \Delta l_0)}{\Delta l_0} \\ &= \frac{d r_0/f_s}{w_0 r_0/f_s}\sin c\left(\pi\frac{f_d}{f_s}\right) = \gamma_w \sin c\left(\pi\frac{f_d}{f_s}\right)\end{aligned}, \tag{9}$$

where $\gamma_w = d/w_0$ is the maximum drum velocity fluctuation rate. It can be seen from Eq. (9) that for a fixed velocity fluctuation frequency the percent maximum line spacing fluctuation is proportional to the percent maximum velocity fluctuation. This is especially significant at very low fluctuation frequency $f_d << f_s$ since $\sin c(\pi f_d/f_s) \cong 1$ and thus $\gamma_l \cong \gamma_w$. Figure 4 shows the effect of percent drum velocity fluctuation and frequencies has on percent maximum line spacing fluctuation when the scanning frequency is set at 2 kHz. It can be seen that with the same velocity fluctuation magnitude, low frequency disturbances tend to induce larger line spacing error.

Effect of Eccentricity

Eccentricity and tooth profile error are sources of gear transmission error. Both contribute to the variation of the instantaneous radius of rotation. In this and the next section, we will investigate their effect on scan line spacing variation.

Suppose the center of rotation of the drum O' deviates from the ideal geometry center O by ε, as shown in Fig. 5. To study the effect of eccentricity we will assume that the scanning frequency and the angular velocity

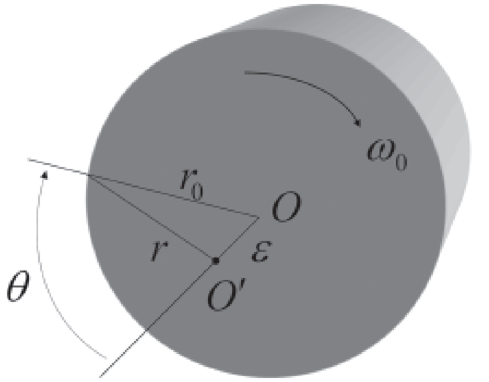

Figure 5. Modeling effect of eccentricity on scan line spacing.

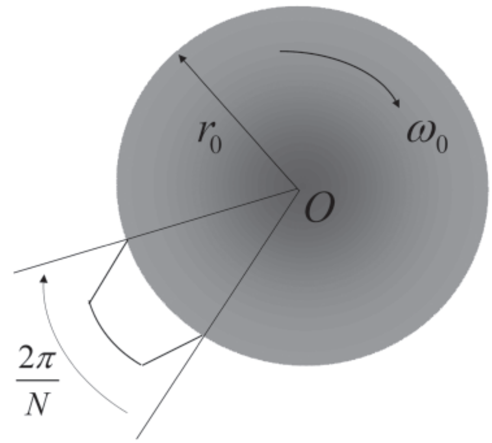

Figure 6. Modeling effect of tooth-profile error on scan line spacing.

are both constants, e.g., w_0 and f_s are constants. From geometry, we can express the instantaneous radius of rotation r and $dr/d\theta$ as

$$r = \sqrt{r_0{}^2 + \varepsilon^2 - 2r_0\varepsilon\cos\theta} \tag{10}$$

and

$$\frac{dr}{d\theta} = \frac{r_0\varepsilon\sin\theta}{\sqrt{r_0^2 + \varepsilon^2 - 2r_0\varepsilon\cos\theta}}. \tag{11}$$

Assuming that the eccentricity is small compared with the nominal radius of rotation, i.e., $r_0 >> \varepsilon$, we have

$$\begin{aligned}
&\sqrt{r^2 + \left(\frac{dr}{d\theta}\right)^2} \\
&= \sqrt{r_0{}^2 + \varepsilon^2 - 2r_0\varepsilon\cos\theta + \frac{r_0^2\varepsilon^2\sin^2\theta}{r_0{}^2 + \varepsilon^2 - 2r_0\varepsilon\cos\theta}} \\
&= \sqrt{r_0^2\left(1 + \frac{\varepsilon^2}{r_0^2} - 2\frac{\varepsilon}{r_0}\cos\theta\right) + \frac{\varepsilon^2\sin^2\theta}{1 + \varepsilon^2/r_0^2 - 2\,\varepsilon/r_0\cos\theta}} \\
&\cong \sqrt{r_0^2\left(1 - 2\,\varepsilon/r_0\cos\theta\right)} \\
&\cong r_0 - \varepsilon\cos\theta.
\end{aligned} \tag{12}$$

The first approximation in the above equation is obtained by neglecting the second order terms, while the last approximation is done using the fact that $(1 + x)^k \cong 1 + kx$ as $x \cong 0$. Substituting Eq. (12) into Eq. (5), we have

$$\begin{aligned}
\Delta l &= w_0\int_{t_0}^{t_0+1/f_s}\sqrt{\left(\frac{dr}{d\theta}\right)^2 + r^2}\,dt \\
&= w_0\int_{t_0}^{t_0+1/f_s}(r_0 - \varepsilon\cos\theta)\,dt.
\end{aligned} \tag{13}$$

Since $\theta = w_0t + \phi$, therefore

$$\begin{aligned}
\Delta l &= \frac{w_0r_0}{f_s} - \varepsilon\sin(w_0t + \phi)\Big|_{t_0}^{t_0+\frac{1}{f_s}} \\
&= \frac{w_0r_0}{f_s} - \varepsilon\left[\sin\left[w_0\left(t_0 + \frac{1}{f_s}\right) + \phi\right] - \sin\left(w_0t_0 + \phi\right)\right] \\
&= \frac{w_0r_0}{f_s} - 2\varepsilon\sin\left(\frac{w_0}{2f_s}\right)\cos\left(w_0t_0 + \phi'\right),
\end{aligned} \tag{14}$$

where $\phi' = w_0/f_s + \phi$. It can be seen that Eq. (14) can also be separated into a nominal line spacing and a variation term due to eccentricity, ε. Further approximation on the variation term can be made if we accept that $f_s >> w_0$, which is a necessary condition for EP processes. Equation (14) can be rewritten as

$$\Delta l = \frac{w_0r_0}{f_s} - \frac{w_0\varepsilon}{f_s}\cos\left(w_0t_0 + \phi'\right). \tag{15}$$

Since for $f_s >> w_0$, $\sin\left(w_0/2f_s\right) \cong w_0/2f_s$, Eq. (15) indicates that the maximum scan line spacing variation due to photoconductor drum eccentricity alone is proportional to the magnitude of the eccentricity. Furthermore, the variation frequency $w_0/2\pi$ is the drum rotating frequency.

Effect of Tooth Profile Error

In this section, the effect of tooth profile error will be studied. Constant scanning frequency and the angular velocity are assumed. Suppose that one end of the photoreceptor drum is a gear with N teeth of equal face width. As shown in Fig. 6, each tooth will span $2\pi/N$ radians around the gear. Within each tooth span, the radius of rotation varies due to imperfect tooth profile. In general, each tooth will have its profile error causing certain amount of variation, $b(\theta)$, on the instantaneous radius of rotation r_0 such that $r = r_0 + b(\theta)$, where $\theta = w_0t + \phi$ is the angular position of the drum. $b(\theta)$ can be restated as

$$b(\theta) = b_i(\theta) \quad \text{for} \quad \frac{2\pi(i-1)}{N} \le \theta < \frac{2\pi i}{N}, \quad i = 1, 2, \ldots, N, \tag{16}$$

where N is the number of teeth. Note that $b(\theta)$ is also periodic, i.e.,

$$b(\theta) = b(\theta + 2\pi). \tag{17}$$

Actual gear measurements[31] suggested that tooth profile error usually introduces transmission error with a fundamental frequency equal to the number of teeth per revolution. The corresponding error magnitude is also much larger than its harmonics at higher frequencies. Thus, without loss of generality, we will restrict the following discussion to the case in which $r = r_0 + b(\theta)$ with $b(\theta) = \beta \sin(N\theta + \varphi)$ and $\theta = w_0 t$, i.e., the radius error is $2\pi/N\theta$ periodic. β is the maximum tooth profile error. Since

$$\frac{dr}{d\theta} = \beta N \cos(N\theta + \varphi), \tag{18}$$

let the instantaneous radius of rotation $R(\theta)$ be

$$\begin{aligned} R(\theta) &= \sqrt{\left(\frac{dr}{d\theta}\right)^2 + r^2} \\ &= \sqrt{\beta^2 N^2 \cos^2(N\theta + \varphi) + r_0^2 + \beta^2 \sin^2(N\theta + \varphi) + 2r_0\beta \sin(N\theta + \varphi)} \\ &= r_0 \sqrt{1 + 2\frac{\beta}{r_0}\sin(N\theta + \varphi) + \frac{\beta^2}{r_0^2}\sin^2(N\theta + \varphi) + \frac{\beta^2 N^2}{r_0^2}\cos^2(N\theta + \varphi)}. \end{aligned} \tag{19}$$

If $r_0 >> \beta$, Eq. (19) can be further simplified to

$$R(\theta) \cong r_0 \sqrt{1 + 2\frac{\beta}{r_0}\sin(N\theta + \varphi) + \frac{\beta^2 N^2}{r_0^2}\cos^2(N\theta + \varphi)}. \tag{20}$$

Substituting Eq. (20) into Eq. (5), the scan line spacing can be calculated as

$$\begin{aligned} \Delta l &= \int_{t_0}^{t_0 + 1/f_s} w_0 R(\theta)\, dt \\ &= w_0 r_0 \int_{t_0}^{t_0 + 1/f_s} \sqrt{1 + 2\frac{\beta}{r_0}\sin(N\theta + \varphi) + \frac{\beta^2 N^2}{r_0^2}\cos^2(N\theta + \varphi)}\, dt \\ &\cong \frac{w_0 r_0}{f_s} \sqrt{1 + 2\frac{\beta}{r_0}\sin(N\theta + \varphi) + \frac{\beta^2 N^2}{r_0^2}\cos^2(N\theta + \varphi)}. \end{aligned} \tag{21}$$

The last approximation in the above equation is based on the fact that the instantaneous radius of rotation $R(\theta)$ does not change during one laser scan period, which is reasonable for an EP engine with high scanning frequency and relatively slow photoreceptor drum angular velocity. When $r_0 >> \beta N$, e.g., when the number of teeth is small, Eq. (21) can be further simplified by neglecting the second order term; i.e.,

$$\begin{aligned} \Delta l &\cong \frac{w_0 r_0}{f_s} \sqrt{1 + 2\frac{\beta}{r_0}\sin(N\theta + \varphi) + \frac{\beta^2 N^2}{r_0^2}\cos^2(N\theta + \varphi)} \\ &\cong \frac{w_0 r_0}{f_s} \sqrt{1 + 2\frac{\beta}{r_0}\sin(N\theta + \varphi)} \\ &\cong \frac{w_0 r_0}{f_s} + \frac{w_0 \beta}{f_s}\sin(N w_0 t + \varphi). \end{aligned} \tag{22}$$

Similar observations can be made from Eq. (22) about the effect of tooth profile error on the scan-line spacing variation as that of the eccentricity. Note that the variation frequency $Nw_0/2\pi$ now equals to the number of teeth per revolution.

Simulation

More complicated analysis can be performed for situations when various error sources are present at the same time. In this case, however, numerical simulation might be more useful in predicting the results. If the instantaneous radius of rotation is given by Eq. (19), the governing equation of the scan line spacing, i.e., Eq. (1) , can be rewritten as

$$\Delta l = \int_{l_0}^{l_0 + \Delta l} dl = \int_{t_0}^{t_0 + 1/f} wR(\theta)\, dt \tag{23}$$

with

$$R(\theta) = \sqrt{(dr/d\theta)^2 + r^2},$$

and

$$r = \sqrt{r_0^2 + \varepsilon^2 - 2r_0\varepsilon\cos\theta} + b(\theta). \tag{24}$$

Note that r now takes into account both eccentricity and tooth profile error.

The numerical simulation results based on a typical 600 dpi monochrome EP engine are shown in Fig. 7. Parameters for the simulation are summarized in Table I. The horizontal axis of the line spacing error spectrum (upper right) is converted to spatial frequency in order to compare with the actual reflectance measurement from the actual printout of the engine. It can be seen that the simulation predicts most of the banding frequencies in the actual printout except for the frequency at 17.2 cycles/in, which is actually a harmonic of the 8.6 cycles/in. Moreover, the disturbance energy at 100 cycles/in, which is due to scanning frequency variation, is usually not visible due to the reduced sensitivity of the human visual system to high spatial frequency.

From Scan Line Spacing to Reflectance

As summarized earlier, researchers[6–10] have developed models that relate the laser dot position error in the process direction (exactly the scan line spacing in the previous discussions) to the exposure on the photoreceptor drum or the reflectance on the printout. Here, we will base our development from the work done by Kacker and co-workers.[29]

The laser dot intensity profile can be modeled as 2-D Gaussian envelope, i.e.,

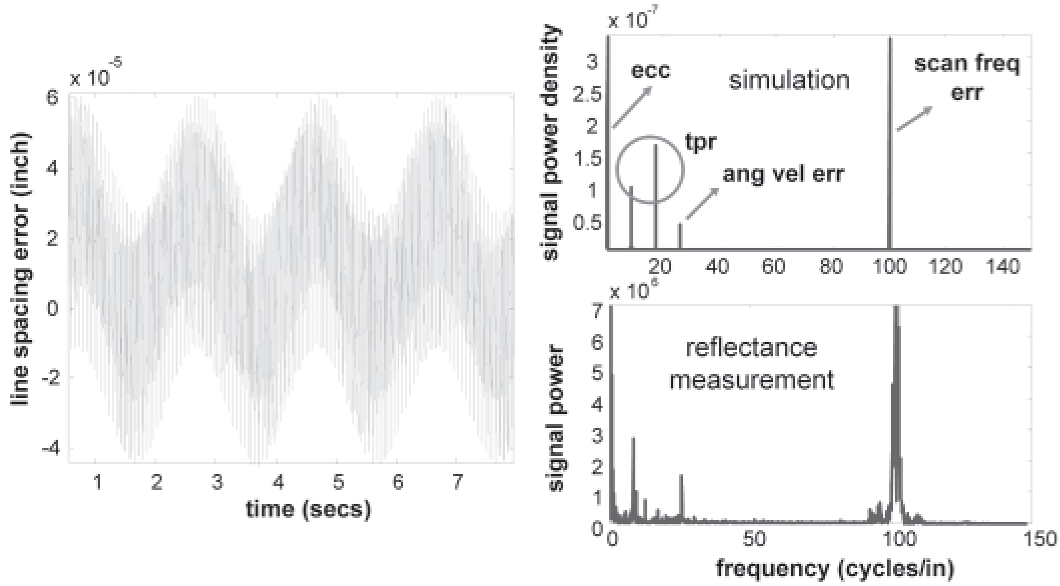

Figure 7. Simulation results of the scan line spacing variation due to various transmission error sources. The actual reflectance measurement is also shown for comparison.

TABLE I. Parameter Set-up for the Scan Line Spacing Simulation

	Platform	4M
Nominal	Radius of rotation r_0 (inch)	1.183/2
	PC drum velocity w_0 (rad/s)	3.141
	Number of teeth N	32
	Scanning period Ts_0 (Hz)	1/1111
Variation	Eccentricity ε (inch)	0.0059
	Velocity variation frequency f_d (Hz)	48
	Velocity variation Δw (rad/s)	0.01
	Scanning period variation ΔTs (sec)	0.01/1111
	Tooth profile error β (inch)	0.003

$$I(x,y) = I_0 \exp\left(-\frac{x^2}{2\sigma_x} - \frac{y^2}{2\sigma_y}\right) \text{Watts}/\text{m}^2, \qquad (25)$$

where x and y are the position in the scan and process direction, respectively. I_0 is the peak intensity of the laser, and σ_x and σ_y are the standard deviations which describe the width of the profile. As we are focusing on effect of the dot positioning error in the process direction, the following 1-D profile will be considered,

$$I(y,t) = I_0(t) \exp\left(-\frac{y^2}{2\sigma_y}\right). \qquad (26)$$

Note that the value of $I_0(t)$ will depend on the switch-on and switch-off time of the laser, which can be expressed as

$$I_0(t) = \begin{cases} 0, & t < 0 \\ I_{\max}(1-\exp(-t/t_r)), & 0 \le t \le t_{\text{off}} \\ I_{\max}(1-\exp(-t_{off}/t_r))(\exp(-t-t_{off}/t_f)), & t > t_{\text{off}} \end{cases} \qquad (27)$$

where it is assumed that the laser is switched on at t = 0 and off at $t = t_{off}$. t_r is the time for the laser intensity to reach $I_{\max}$ and t_f is the time for the intensity to fall back to 0. The exposure value at position y due to the n-th printed pixel along the process direction at position y_n can be computed by

$$E_n(y) = \int_0^{\infty} I_0(\tau) \exp(-\frac{(y-y_n)^2}{2\sigma_y^2}) d\tau \quad \text{J}/\text{m}^2. \qquad (28)$$

Assuming that the contributions of each printed pixel to the total exposure on the photoreceptor drum is additive, the total exposure value at y may be found by

$$E(y) = \sum_n E_n(y). \qquad (29)$$

The relation among the exposure on the photoreceptor drum, toner mass transferred during development stage and the final reflectance/absorptance at any fixed position on the page is quite complicated. However, a static nonlinear mapping $\gamma(\cdot)$ between the exposure $E(y)$ on the photoreceptor drum and the reflectance $R(y)$ on the paper can be obtained experimentally, i.e.,

$$R(y) = \gamma(E(y)). \qquad (30)$$

A typical γ curve can be found in Kacker's study.[29]

To obtain the model from transmission error to halftone banding, first note that the position of the n-th scan line, y_n, can be expressed as

$$y_n = \int_0^{\frac{n}{f_s}} w \sqrt{\left(\frac{dr}{d\theta}\right)^2 + r^2}\, dt, \qquad (31)$$

which is based on Eq. (5). Substituting Eq. (31) into (28) and use Eq. (29) and (30), we have

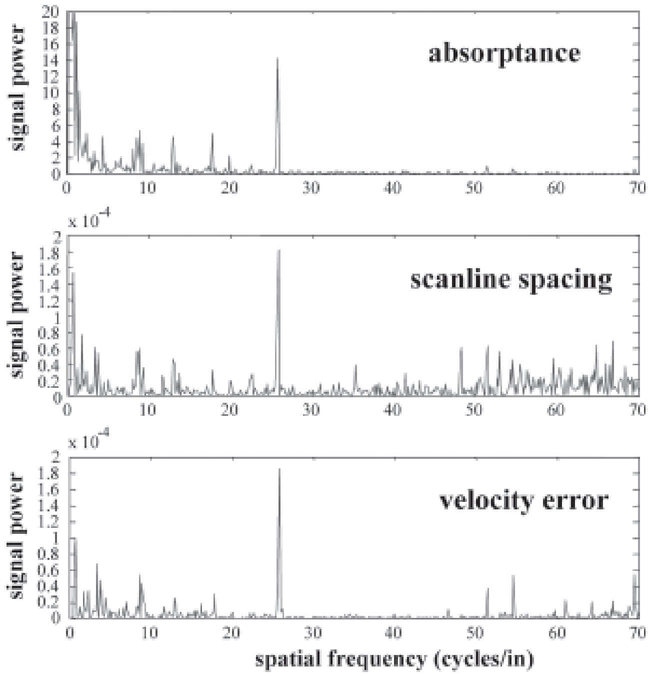

Figure 8. Spectra of the measured average absorptance, scanned line spacing and the rastering line spacing.

$$R(y) = \gamma\left(\sum_n \int_0^\infty I_0(\tau)\exp\left(-\frac{y-\int_0^{n/f_s} w(t)\sqrt{(dr/d\theta)^2+r(t)^2}\,dt)}{2\sigma_y^2}\right)d\tau\right) \quad (32)$$

Equation (32) is a complete model that maps the transmission parameters such as scanning frequency, angular velocity, and radius of rotation to the output reflectance on a printed page. Numerical simulation can be performed based on this equation to help us investigate the relationship among those parameters, which is not the main focus of this study. The close correlation among angular velocity variation, line spacing variation, and reflectance variation can also be verified by comparing the actual measurements. Figure 8 shows the frequency spectrums of the measured velocity error, line spacing variation, and reflectance variation for a typical 600 dpi laser platform. We observe similarity of those three frequency spectrums in the frequency region from 5 to 30 cycles/in. This indicates that angular velocity fluctuation has direct effect on output reflectance variation, which implies that control of the photoreceptor drum angular velocity could reduce banding artifact.

Controller Design

Closed-Loop OPC Drum Velocity Regulation

As described previously, the imaging part of most monochrome laser printing systems consists of two subsystems (see Fig. 2). The first subsystem forms a motor/gear-train transmission system, which is composed of the main motor drive with onboard driver, the gear train and the OPC drum. Phase-lock loop (PLL) is the most common method of velocity control for BLDC motors. The PLL is a feedback system composed of a phase comparator, a low-pass filter, an error amplifier in the forward signal path, and a pulse generator in the feedback path. The desired angular velocity is proportional to the frequency of the reference pulse generated by the oscillator. The motor angular velocity is proportional to the frequency of the frequency generator (FG) pulses generated by the Hall-effect sensors. The phase comparator compares the phase differences between these two signals and generates an error signal proportional to the phase difference. The phase error is then passed through the low-pass filter and the amplifier to set voltage level for the PWM generator, which will modulate the amount of current flowing through the phase windings and adjust the motor velocity.

Note that the PLL is to regulate the speed of the motor and not that of the photoconductor drum. Since the motor shaft, the gear train and the photoconductor drum are not rigidly coupled, constant motor speed does not guarantee constant photoconductor drum velocity. That is, the Hall-effect sensor will not be able to pick up the disturbances introduced between the motor and the photoconductor drum. This is demonstrated by observing the signal from the Hall-effect sensor and that of the optical encoder mounted on the photoconductor drum, see Fig. 9. Therefore, to compensate for the disturbances that cause photoconductor drum velocity fluctuation, it would be desirable to regulate the photoconductor drum velocity by directly measuring the drum velocity or position.

A schematic of the proposed closed-loop system is depicted in Fig. 10. Two separate controllers are to be designed based on the transfer function from control effort, $u(s)$, to the angular velocity error, $e(s)$, which is the called plant transfer function. A 3rd order model is fitted to the experimental frequency response of the plant as having the following transfer function:

$$G_0(s) = \frac{2.046\times 10^7}{s^3 + 801.3\,s^2 + 4.443\times 10^5 s + 4.326\times 10^6}. \quad (33)$$

The loop shaping controller forms the first layer control, which will reject those non-periodic disturbances lying within the low frequency region. Note that this layer of control also aims at eliminating the dc component of the disturbances so that the frequencies of the remaining periodic components will be stationary. The repetitive controller then forms the second layer of control to cancel those periodic disturbances. The input to the controllers, $e(s)$, is the angular velocity error of the OPC drum measured by an optical encoder and the control effort $u(s)$ to the motor driver are summation of the computed outputs from both controllers.

Synthesis of the HVS Shaped H_∞ Loop-shaping Controller

The guideline for H_∞ loop-shaping design is available in many existing literatures.[30] The objective is to design feedback controllers such that the open-loop transfer function has high gain at the specific frequencies where disturbances are to be rejected. The human contrast sensitivity function (CSF) is a good target for shaping the open loop transfer function gain where high gain is required to reduce the perceived banding (with high contrast sensitivity). It also provides a guideline for reducing

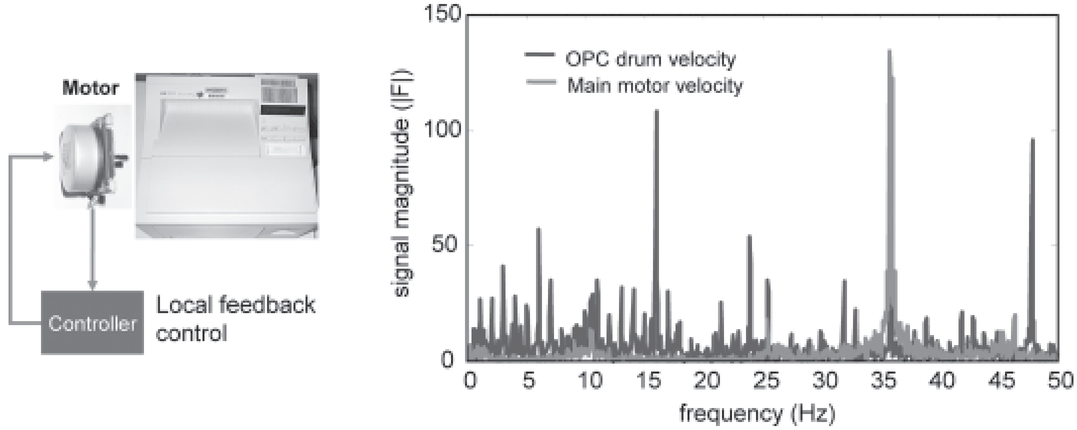

Figure 9. Velocity fluctuation comparison between the photoconductor drum and the main drive motor.

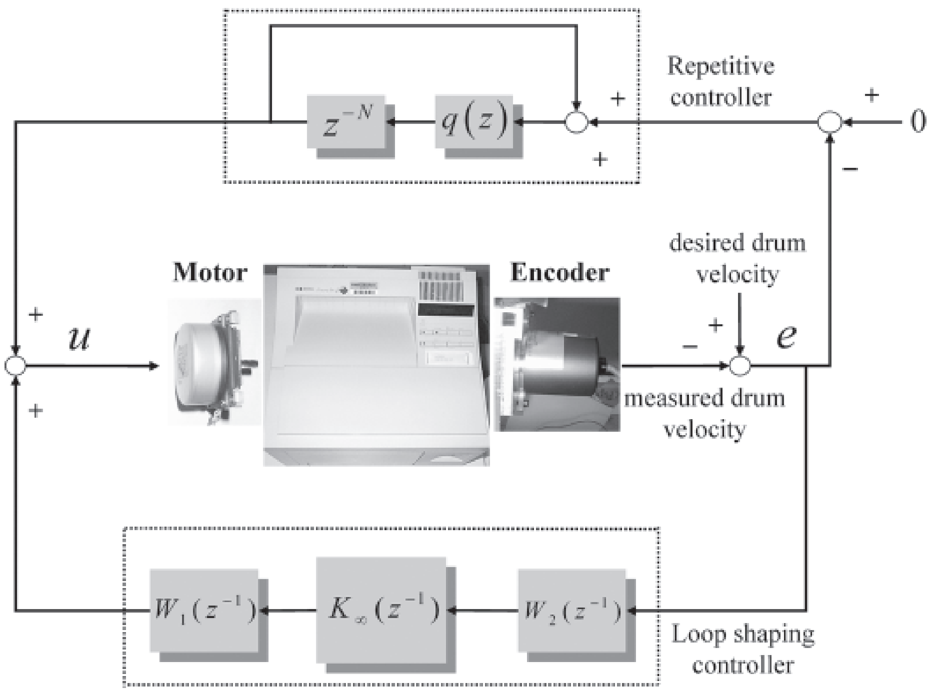

Figure 10. Configuration of the proposed two-level closed-loop control system.

the open-loop transfer function gain to provide robustness for actuator bandwidth limitation and model uncertainty. There are various versions of CSF functions in the existing literature,[11,12] which all represent certain band-pass or low pass characteristics, see Fig. 11. In particular Barten's low-pass model, which is modified from Mannos' model, can be parameterized to be[12]

$$\begin{aligned} CSF(f_1) &= a \times (b + cf_1) e^{\left\{-(cf_1)^d\right\}}, \ \text{if } f_1 \geq f_{\max} \\ CSF(f_1) &= a \times (b + cf_{\max}) e^{\left\{-(cf_{\max})^d\right\}}, \ \text{if } \ f_1 < f_{\max} \end{aligned} \tag{34}$$

with a = 2.6, b = 0.0192, c = 0.114, d = 1.1. In addition,

$$f_1 = \frac{f \times \pi}{360 \times \tan^{-1}(1/2v_d)}, \tag{35}$$

where v_d is the viewing distance in inch, f is the spatial frequency in cycles/in, and f_1 is in cycles/deg. Note that $f_{\max}$ satisfies the following equation:

$$1 - bc^{d-1} df_{\max}{}^{d-1} - c^d df_{\max}{}^{d} = 0. \tag{36}$$

From a feedback control design point of view, a certain amount of low frequency gain is needed to maintain an acceptable steady state operating speed regulation. Hence, Barten's modified CSF would be a better interpretation of the desired frequency dependent magnitude profile of the open-loop transfer function of the OPC drum velocity control system.

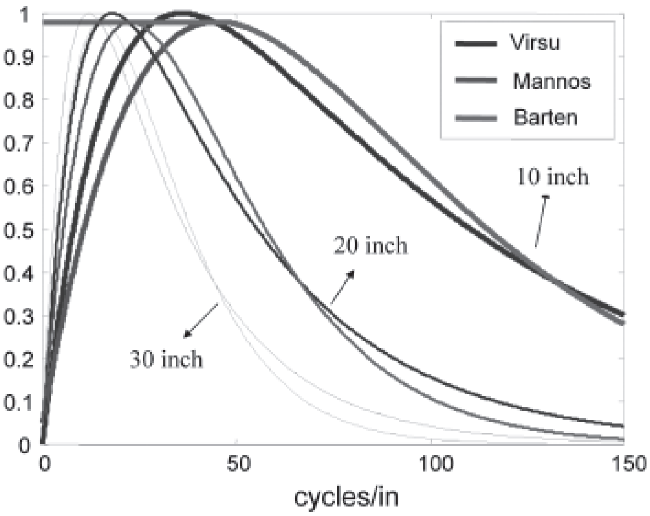

Figure 11. Various versions of CSF at different viewing distances.

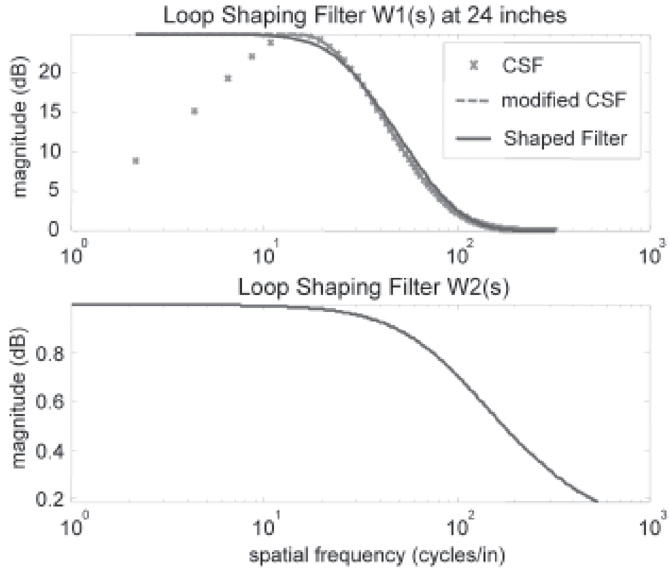

Figure 12. Frequency responses of the weighting filters.

An H_∞ loop-shaping approach will be employed to design a suitable controller for the first layer control. The design process is briefly summarized as follows. The precompensator $W_1(s)$ and post-compensator $W_2(s)$ are properly chosen to shape the loop transfer function of the augmented plant $P_s(s) = W_2(s)G_0(s)W_1(s)$ into the desired loop transfer function. The loop shaping controller that is needed to achieve the desired open loop transfer function, $K_\infty(s)$, is then found by solving the following minimization problem:

$$\gamma_{opt} = \inf_{K_\infty \text{ stabilizing}} \left\| \begin{matrix} (I+P_sK_\infty)^{-1} & (I+P_sK_\infty)^{-1}P_s \\ K_\infty(I+P_sK_\infty)^{-1} & K_\infty(I+P_sK_\infty)^{-1}P_s \end{matrix} \right\|_\infty . \tag{37}$$

The actual feedback controller $K(s)$ is formed by combining $W_1(s)$, $W_2(s)$ and $K\infty(s)$, i.e., $K(s) = W_1(s)K\infty(s)W_2(s)$. Typically, $W_1(s)$ is chosen to satisfy the performance requirements and $W_2(s)$ is selected to satisfy stability and robustness considerations. In this case, $W_1(s)$ is chosen to be a stable and minimum phase filter that approximates Barten's CSF with a viewing distance of 24 inches. $W_2(s)$ is chosen as a strictly proper filter which rolls off the controller gain at high frequency. The orders of $W_1(s)$ and $W_2(s)$ are chosen to be as low as possible to avoid producing high order controller. After some iteration, two acceptable filters are found to be

$$W_1(s) = \frac{s^2 + 1579\,s + 1.374\times10^6}{s^2 + 392.4s + 7.757\times10^4} \tag{38}$$

and

$$W_2(s) = \frac{1}{0.0008595s + 1}. \tag{39}$$

Figure 12 shows the frequency responses of the two filters. Note that $W_1(s)$ is selected to emphasize gain increase up to around 100 cycles/in, since this is the region where the disturbances are most significant. The resulting feedback controller is an 8th order compensator described by Eq. (40).

$$K(s) = \frac{3817\mathrm{s}^7 + 1.351\times10^7\mathrm{s}^6 + 2.279\times10^{10}\mathrm{s}^5}{\mathrm{s}^8 + 4283\mathrm{s}^7 + 8.072\times10^6\mathrm{s}^6 + 9.265\times10^9\mathrm{s}^5} \frac{+2.253\times10^{13}s^4 + 1.382\times10^{16}s^3}{+7.337\times10^{12}\mathrm{s}^4 + 4.063\times10^{15}\mathrm{s}^3} \frac{+5.942\times10^{18}s^2 + 1.422\times10^{21}s + 1.698\times10^{23}}{+1.492\times10^{18}\mathrm{s}^2 + 3.111\times10^{20}\mathrm{s} + 3.279\times10^{22}}. \tag{40}$$

Synthesis of the Repetitive Controller

In discrete time domain, any periodic signal with fundamental period of N can be generated by a series of delay taps with unity positive feedback and a set of nonzero initial conditions. This structure, combined with the internal model principle, has been the kernel of digital repetitive control. Theoretically, a discrete time repetitive controller is capable of rejecting periodic disturbances and their harmonics up to the Nyquist frequency. There are many ways to incorporate a repetitive controller into feedback or feedforward loop design. In the following, we will synthesize the repetitive controller proposed by Tomizuka.[27]

Consider the representation of a closed-loop system, which is the transfer function from the controller input to the velocity error output after implementing the nominal loop controller, i.e., the loop shaping controller $K(s)$ described in the previous section. Figure 13 illustrates the scheme for identifying the closed-loop system, which can be expressed as

$$G_c(z^{-1}) = \frac{z^{-d}B(z^{-1})}{A(z^{-1})} = \frac{z^{-d}B^+(z^{-1})B^{-1}(z^{-1})}{A(z^{-1})}, \tag{41}$$

where d is the number of delay periods in the system. $B^+(z^{-1})$ and $B^-(z^{-1})$ are parts of $B(z^{-1})$ with the cancelable and uncancelable (unstable or oscillatory) zeros, respectively. It is known that the prototype repetitive controller $G_r(z)$ can be synthesized as

$$G_r(z^{-1}) = k_r\, R\left(z^{-1}\right)\Big/ S\left(z^{-1}\right) \frac{z^{-N}}{1 - z^{-N}}, \tag{42}$$

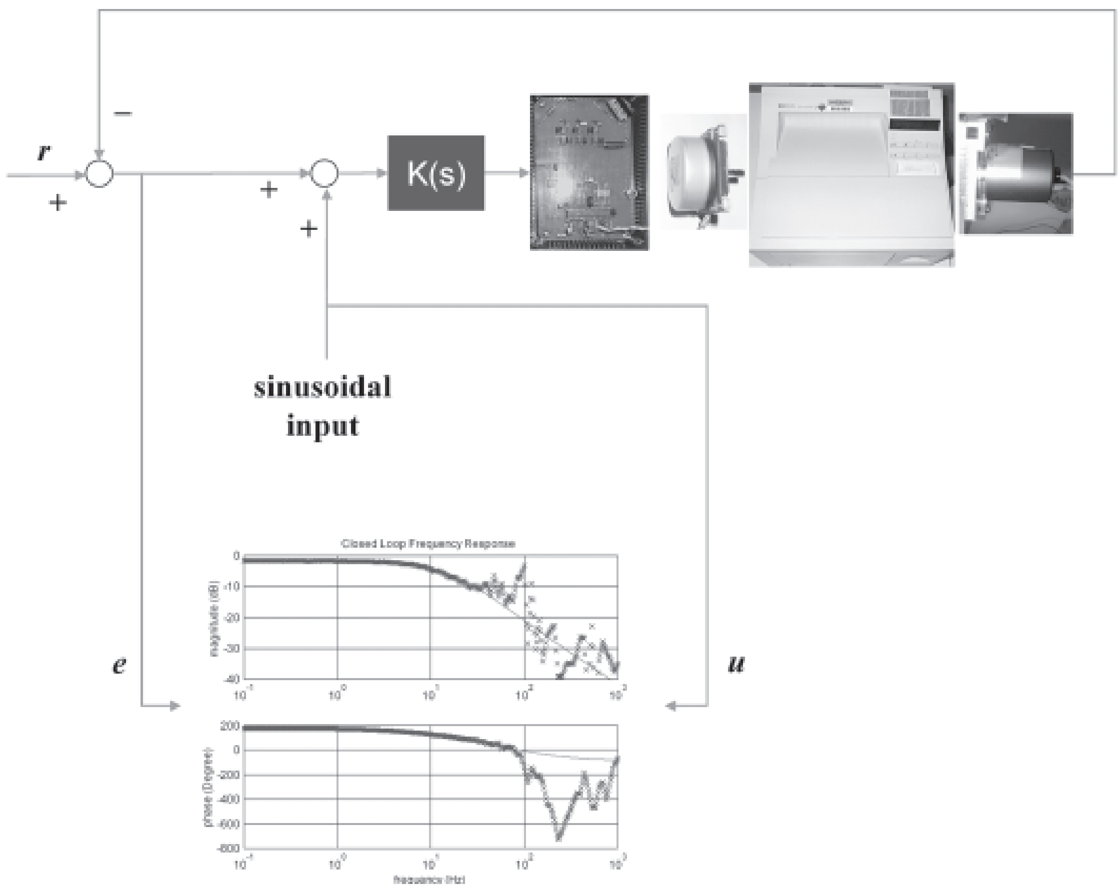

Figure 13. Identification of the closed-loop system. The frequency response to be identified is from the added external signal to the summing junction of the controller input to the velocity error.

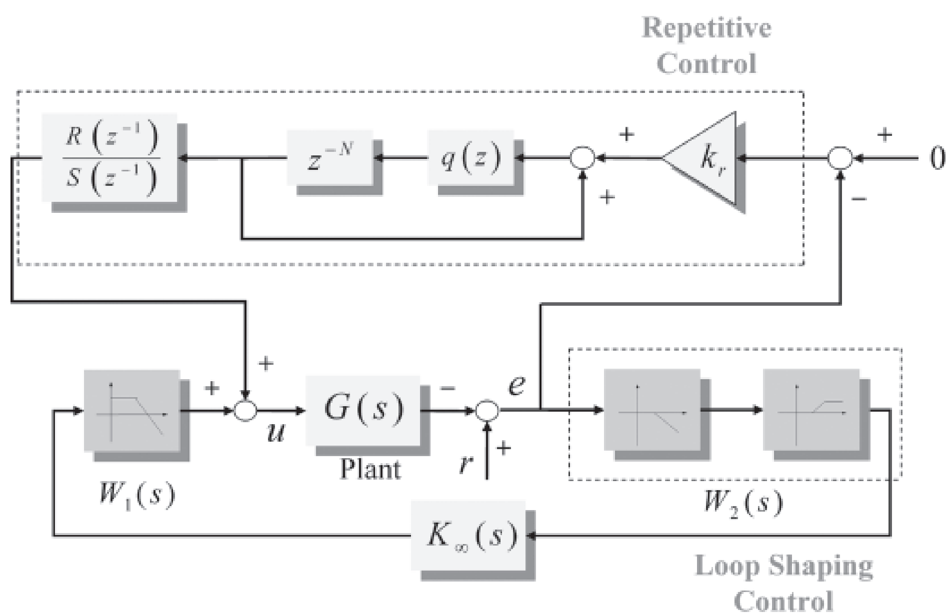

Figure 14. Proposed two-level repetitively controlled closed-loop system.

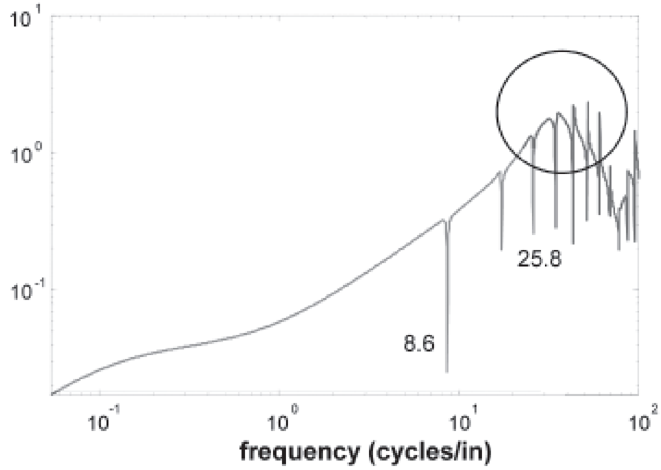

Figure 15. Frequency response of the sensitivity function for the repetitively controlled closed-loop system.

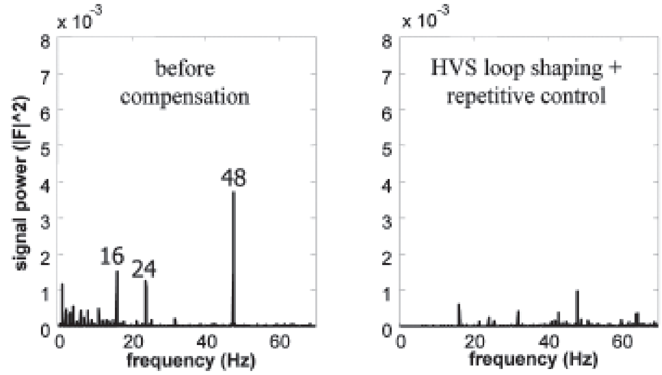

Figure 16. OPC drum velocity variation spectrum before compensation and after being compensated using the proposed two-level control. The mean values were subtracted from both velocity data before applying Fourier analysis.

where

$$R\left(z^{-1}\right) = k_r z^{d} A\left(z^{-1}\right) B^{-}(z),$$

$$S\left(z^{-1}\right) = B^{+}\left(z^{-1}\right) b,\ b \geq \max\left|B^{-}\left(e^{-jw}\right)\right|^2,\ w \in [0, \pi].$$

with $N = f_s/f_d$, where f_s is the sampling frequency of the discrete time system and f_d is the fundamental frequency of disturbances to be rejected. For stability, k_r is limited to $0 < k_r < 2$. A zero-phase error low pass q-filter, $q(z) = (z^{-1} + a + z)/(a + 2)$ with $a \in Z^{+}$, is introduced in the forward or feedback loop of the delay taps to improve stability robustness.

Experimental Results

The proposed two-level closed-loop control system is shown in Fig. 14. The control scheme is applied to the experimental platform, a 600 dpi monochrome laser printer. A high-resolution optical encoder capable of 50,000 pulses per revolution is mounted on the OPC drum. The sampling frequency of the experimental system is set to 1000 Hz. After activating the loop- shaping control, the closed-loop system, $G_c(z)$, is identified as Eq. (43):

$$G_c(z^{-1}) = \frac{z^{-1}\left(-0.01957 + 0.07826\, z^{-1} - 0.1437\, z^{-2} + 0.1197\, z^{-3} - 0.03519 z^{-4}\right)}{1 - 4.2971\, z^{-1} + 7.7448\, z^{-2} - 7.3329\, z^{-3} + 3.6426\, z^{-4} - 0.7569 z^{-5}}. \tag{43}$$

Note that the one step delay z^{-1} comes from discretizing the identified continuous-time system into its zero-order-hold (ZOH) equivalent discrete time model. Following the synthesis procedure, the repetitive controller is design to be

$$G_r\left(z^{-1}\right) = k_r \cdot \frac{z^{-N+d+1}}{1 - z^{-N}} \cdot \frac{R\left(z^{-1}\right)}{S\left(z^{-1}\right)}, \tag{44}$$

where

$$k_r = 0.12,\ d = 2,$$

and

$$R(z^{-1}) = (1 - 4.2971 z^{-1} + 7.7448 z^{-2} - 7.3329 z^{-3} + 3.6426 z^{-4} - 0.75688 z^{-5})(2.86761 - 2.3873 z^{-1} + z^{-2})$$

$$S(z^{-1}) = -0.01957 + 0.03154 z^{-1} - 0.01227 z^{-2}$$

Since the fundamental frequency of the repetitive disturbances after closing the loop using the loop shaping controller is 8 Hz, the period of the repetitive controller N should be set to $N = 1000/8 = 125$. To improve overall system robustness, $a = 2$ is chosen for the q-filter, i.e.,

$$q(z) = \frac{z^{-1} + 2 + z}{4}. \tag{45}$$

Figure 15 shows the frequency response of the sensitivity function for the overall repetitively controlled system from output disturbance to velocity. It can be seen that system sensitivity is significantly reduced at the frequency region up to around 30 cycles/in with the help of the loop-shaping controller. This is achieved by sacrificing some performance at certain high frequency region. However, the repetitive controller is able to reject the periodic disturbances even at the high frequency regions. In the experiment, the repetitive controller was activated after the loop shaping controller was started. Figure 16 shows the comparison of the frequency spectrums for the velocity errors before compensation and with the loop shaping plus the repetitive controller. It can be seen that the loop-shaping controller reduced the disturbances located at the low frequency region, and the repetitive controller significantly reduced the disturbances at 16, 24, and 48 Hz, which correspond to 8.6, 12, and 25.8 cycles/in, respectively. The reduction effect on the visual banding was further verified by measuring the frequency spectrum of the reflectance on a printed image, as shown in Fig. 17, and by observing the printed images

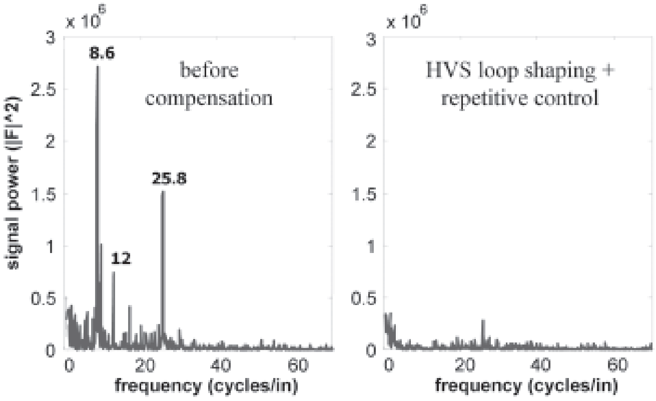

Figure 17. Reflectance measurement from the printout before compensation and after being compensated using the proposed two-level control.

from the uncompensated and the compensated systems, as shown in Fig. 18. It is seen that significant banding reduction was attained after implementing the HVS based loop-shaping repetitive control.

Conclusion

A closed-loop controller design for banding artifact reduction was proposed for EP process in this study. Strong correlation between the velocity variation of the photoconductive drum and the reflectance variation on the printed image was verified through system modeling, signal processing, and experimental measurement. This motivated closed-loop velocity control of the OPC drum for banding reduction. The proposed control strategy included two levels of OPC drum speed regulation. The first level utilized an H_∞ loop-shaping technique to incorporate the human contrast sensitivity into the control loop to eliminate low frequency and non-periodic drum velocity fluctuation. The second level applied an internal model based repetitive controller to reduce the effect of periodic velocity fluctuations. Effectiveness of the proposed approach was verified by experimental results.

It should be pointed out that the proposed design is not limited to the monochrome platform. Existence of multiple imaging components in color platforms might necessitate the utilization of multiple actuators and sensors, as is currently under investigation. Furthermore, although a high-resolution encoder is used in the discussion, the necessary encoder resolution has been found to be at least an order of magnitude less than the one used in this study. Finally, other linear control algorithm can also be considered for the nominal loop controller design.

Acknowledgment. We gratefully acknowledge support from the Hewlett-Packard Company.

Figure 18. Actual printouts before and after compensation. Significant banding reduction can be seen in the bottom compensated image.

References

1. T. Kusuda, M. Ikeda, T. Ogiri, and T. Besshi, Transmission deviation caused by eccentricity in multi gear systems, *Proc. PICS,* IS&T, Springfield, VA, 1999, pp. 119–124.
2. H. Kawamoto, Rotor dynamics of polygonal mirror scanner motor supported by air bearings in digital electrophotography, *J. Imaging Sci. Technol.* **41,** 565 (1997).
3. H. Kawamoto, Transient vibration of a laser scanner motor in digital electrophotography, *Proc. PICS 2000,* IS&T, Springfield, VA, 2000, pp. 17–21.
4. H. Kawamoto, Chatter vibration of a cleaner blade in electrophotography, *J. Imaging Sci. Technol.* **40,** 8 (1996).
5. H. Kawamoto, K. Udagawa and M. Mori, Vibration and noise induced by electrostatic force on a contact charger roller of electrophotography, *J. Imaging Sci. Technol.* **39,** 477 (1995).
6. P.D. Burns, M. Rabbani and L.A. Ray, Analysis of image noise due to position errors in laser writers, *Applied Optics* **25,** 2158 (1986).
7. P. Melnychuck and R. Shaw, Fourier spectra of digital halftone images containing dot position errors, *J. Opt. Soc. Amer.* **5,** 1328 (1988).
8. D. D. Haas, Contrast modulation in halftone images produced by variation in scan-line spacing, *J. Imaging Technol.* **15,** 46 (1989).
9. R. P. Loce, W. L. Lama and M. S. Maltz, Modeling vibration-induced halftone banding in a xerographic laser printer, *J. Electronic Imaging* **4,** 48 (1995).
10. R. Loce and W. Lama, Halftone banding due to vibrations in a xerographic image bar printer, *J. Imaging Technol.* **16,** 6 (1990).
11. J. L. Mannos and D. J. Sakrison, The effects of a visual fidelity criterion on the encoding of images, *IEEE Trans on Information Theory*, **IT-20,** 525 (1974).
12. P. Barten, Evaluation of subjective image quality with the square-root integral method, *J. Opt. Soc. Amer.* **7,** 2024 (1990).
13. Y. Hotta, M. Goto, and T. Miyamoto, Image forming apparatus having relationship between driving gear pitch and scanning line pitch, US Patent 5,917,529 (1999).
14. P. L. Jeran, Gear train control system for reducing velocity induced image defects in printers and copiers, US Patent 5,812,183 (1998).
15. R. J. Lawton and D. R. Marshall, Beam deflecting for resolution enhancement and banding reduction in a laser printer, US Patent 5,920,336 (1999).
16. W. E. Foote and R. G. Sevier, Laser printer with apparatus to reduce banding by servo adjustment of a scanned laser beam, US Patent 5,760,817 (1998).
17. K. Bannai, Image forming apparatus with anti-banding implementation, US Patent 5,315,322 (1994).
18. M. T.-S. Ewe, J. M. Grice, G. T.-C. Chiu, J. P. Allebach, C.S. Chan, and Wayne Foote, Banding reduction in electrophotographic process using piezoelectric actuated laser beam deflection device, *Proc.*

NIP 16: International Conference on Digital Printing Technologies, IS&T, Springfield, VA, 2000, pp. 276–280.
19. R. P. Loce and W. L. Lama, Printer compensated for vibration-generated scan line errors, US Patent 4,884,083 (1989).
20. D. W. Costanza, R. E. Jodoin, and R. P. Loce, Method and apparatus for compensating for raster position errors in output scanners, US Patent 5,900,901 (1999).
21. R. D. Morrison, System and method for modifying an output image signal to compensate for drum velocity variations in a laser printer, US Patent 5,729,277 (1998).
22. W. L. Lama, R. P. Loce, and J. A. Durbin, Image bar printer compensated for vibration-generated scan line errors, US Patent 4,801,978 (1989).
23. G.-Y. Lin, J. M. Grice, J. P. Allebach, G. T.-C. Chiu, W. Bradburn, and J. Weaver, Banding artifact reduction in electrophotographic printers by using pulse width modulation, *Proc. NIP 16: 2000 International Conference on Digital Printing Technologies*, IS&T, Springfield, VA, 2000, pp. 281–286.
24. C.-H. Li and J. Shu, Banding noise reduction for clustered-dot dither, US Patent 5,875,287 (1999).
25. J. Marsden, Reduction of banding in printed images, US Patent 6,025,922 (2000).
26. S. Hara, Y. Yamamoto, T. Omata, and M. Nakano, Repetitive control system: A new type servo system for periodic exogenous signals, *IEEE Trans. Automatic Control* **33,** 659 (1988).
27. M. Tomizuka, T. C. Tsao, and K. K. Chew, Analysis and synthesis of discrete time repetitive controllers, *ASME J. Dynamic Systems, Measurements and Control* **111,** 353 (1989).
28. L. B. Schein, *Electrophography and Development Physics*, Laplacian Press, Morgan Hill, California, USA, 1996.
29. D. Kacker, T. Camis, and J. P. Allebach, Electrophotographic process embedded in direct binary search, *Proc. SPIE*, **3963,** 468, (2000).
30. K. Glover and D. Mcfarlane, Robust stabilization of normalized coprime factor plant descriptions with H•-bounded uncertainty, *IEEE Trans. Automatic Control* **34,** 821 (1989).
31. J. D. Smith, *Gear Noise and Vibration*, Marcel Dekker, New York, New York, 1999.